Shear-Lag Model for a Single Fiber Metal Matrix Composite with an Elasto-Plastic Matrix and a Slipping Interface

S. Mahesh [a,*], J. C. Hanan [b], E. Üstündag [b], I. J. Beyerlein [c],

[a] *Materials Science and Technology Division,*

Los Alamos National Laboratory, Los Alamos, NM 87545. USA.

[b] *Department of Materials Science,*

California Institute of Technology, Pasadena, CA 91125. USA.

[c] *Theoretical Division,*

Los Alamos National Laboratory, Los Alamos, NM

Abstract

We present a shear-lag stress analysis methodology which accounts for both matrix strain-hardening plasticity and interfacial slip in a single fiber metal matrix composite (MMC) subjected to uniaxial tensile loading and unloading along the fiber direction. The fiber may either be broken or intact. Among other things, the model predicts residual stress and strain distribution after a cycle in the fiber and matrix. The development of the model is motivated by the recent measurement (Hanan *et al* [1]) of elastic strain evolution with loading in each phase of an Al_2O_3/Al composite using neutron diffraction. The model also estimates two crucial *in-situ* material parameters using these measurements, which cannot be obtained from bulk tests: the frictional threshold of the interface, and the *in-situ* yield point of the matrix. With these parameters, the predicted elastic strain evolution with loading is in

excellent agreement with the experimental data.

Key words: metal matrix composites, damage mechanics, shear-lag model, interfacial slip, matrix plasticity

1 Introduction

Shear-lag models are often used for fast computational stress analysis of large unidirectional fiber-reinforced composites with partial damage. The superior computational efficiency of these models relative to e.g., three-dimensional finite element analysis, stems in part from the simplifying assumption of one-dimensional displacement and stress fields. Shear-lag models do not provide detailed information about the spatial variations of stresses and displacement within the composite. Nevertheless, they capture the average stress field over fiber and matrix cross-sections accurately enough for purposes of material failure predictions. An application where shear-lag stress analysis is preferred over more detailed methods on account of its speed arises in the statistical study of composite strength distributions through Monte-Carlo simulations (see Mahesh *et al* [2] and references therein). In these studies, one simulates damage evolution in composite specimen containing a few thousand fibers. Stress analysis, which must be repeated at each incremental damaged state is the slowest step of this computationally intensive procedure, and shear-lag models are presently the fastest way to execute it.

Shear-lag models for unidirectional composites vary in their degree of com-

* Corresponding author.
Email address: mahesh@lanl.gov (S. Mahesh).

plexity. Some models pertain to single fiber composites, while others apply to multi-fiber composites with various fiber arrangements (2D, 3D square / hexagonal lattice / random arrangement). The material behavior of the composite constituents, viz., fiber, matrix and interface constitutive laws and loading conditions (monotonic / cyclic, mechanical / thermal / thermomechanical) also distinguish different shear-lag models.

The first *single fiber* shear-lag model was developed by Cox [3]. He considered a broken elastic fiber embedded in an elastic matrix with a perfectly bonded interface and loaded in tension along the fiber direction. Aveston and Kelly [4] and Budiansky *et al* [5] extended Cox's model as a part of their multi-fiber composite model to the case that the interface may debond and slip if the interfacial shear stress exceeds a certain threshold. More recently, Cox's model has been considerably refined by Hsueh [6,7] for bonded, and debonding interfaces. In Hsueh's solution, the displacement and stress fields in the fiber and matrix show both axial and radial variation and exactly satisfy certain boundary conditions only approximately satisfied by Cox's solution. The shear-lag model of Hsueh *et al* [8] includes the effect of thermal residual stresses in a composite with an elastic fiber and matrix and a bonded interface.

The case of a *multi-fiber* unidirectional composite tape with stiff elastic fibers embedded in a compliant elastic matrix and subjected to tension along the fiber direction was first analyzed and solved by Hedgepeth [9] in the shear-lag framework. Hedgepeth's model, applicable best to a polymer matrix composite, assumes a perfectly bonded interface and a compliant matrix incapable of carrying tensile load. Since this pioneering work, shear-lag models have been developed for a variety of different fiber-matrix-interface constitutive combinations, fiber arrangement geometries, and loading conditions. Hedgepeth

and Van Dyke [10] extended the model to account for three-dimensional fiber composites in which the fibers are arranged in a hexagonal or square lattice. Landis *et al* [11] developed a model for the case of a matrix with non-negligible stiffness and which therefore also carries tensile load. Lagoudas *et al* [12] and Beyerlein and Phoenix [13] extended the shear-lag model to the case of a composite with elastic fibers, viscoelastic matrix and bonded interface.

The present work is motivated by a recent experiment by Hanan *et al* [1]. They cyclically loaded in tension a single Al_2O_3 fiber / Al matrix composite and measured the elastic strain separately in the fiber and the matrix, using neutron diffraction. The fiber was broken at the mid-point of the composite. Preliminary analysis reported in [1] suggests that the important damage events in this experiment are fiber fracture, matrix yielding and strain-hardening, and interfacial debonding. The primary goal of the present work is to obtain a deeper understanding through modeling, of the damage evolution in this composite (especially matrix plasticity and interfacial slip evolution) during this experiment. It is assumed that an elastic fiber is embedded in a ductile linear strain-hardening plastic matrix with non-negligible tensile stiffness relative to the fiber. Frictional slip, with a prescribed shear threshold is assumed to occur at the interface. The stress response in the course of one load-unload cycle of axial tension along the fiber direction is described in Sections 2 and 3. Residual strains are not considered, i.e., further load cycling in the model does not result in a different stress evolution from the original cycle. Strain predictions of the present model are compared with measured values in Section 4 for model validation.

Despite its approximate nature, we pursue a shear-lag approach rather than axisymmetric finite element calculation to interpret the Hanan *et al* experi-

ment for two reasons. First, we anticipate numerical difficulties in the finite element calculations due to the concurrence of the crack-tip field, extensive plasticity in a ductile matrix and interfacial slipping near the fiber fracture. These difficulties, which may need ad-hoc assumptions (e.g., artificial crack blunting) to overcome in the finite element calculation, can be handled elegantly in the shear-lag model as will be seen in Sections 2 and 3 below. Nevertheless, such a detailed axisymmetric calculation, left to later work, would be valuable in further validating the shear-lag model presented here. Second, once developed and validated, it is a conceptually straightforward task to extend the present single fiber shear-lag model to a multi-fiber composite. The multi-fiber composite model, will be of greater practical use than a corresponding three-dimensional finite element model, as stated at the beginning of this section. Such an extension is also left to future work.

2 Shear-Lag Model of Monotonic Loading

2.1 Geometric and Kinematic Assumptions

The model composite of length 2ℓ consists of a single cylindrical fiber of radius a encased in a cylindrical matrix of radius b as shown in Figure 1a and is loaded in tension along the fiber (z) direction. Load is applied to the matrix at $z = \pm\ell$. For purposes of modeling, we follow Aveston and Kelly [4] and Budiansky *et al* [5] and separate the matrix into distinct parts. We term these the *tensile matrix* and *shear matrix* as shown in Figure 1b, and assume they are loaded in pure axial stress and pure shear stress, respectively. The tensile matrix has a cross-sectional area of $\pi(b^2 - a^2)$ and is assumed to be situated at radial

coordinate $r = \bar{R}$, $a < \bar{R} \leq b$. The two works cited above assign different meanings to the quantity $\bar{R}$: Aveston and Kelly [4] regard it as the radius where the matrix z-displacement equals the average z-displacement of the cross-section, while Budiansky *et al* [5] give it an energy interpretation. In the present model, we will take $\bar{R} = (a+b)/2$, since the results are not sensitive to its precise value except when $\bar{R}/a \approx 1$. This value for $\bar{R}$ corresponds to Aveston and Kelly's prescription if we assume the matrix z-displacement varies linearly in a cross-section.

As stated in the introduction, shear-lag models typically treat displacements as one-dimensional fields. Accordingly, let $w_f(z)$, and $w_{tm}(z)$ denote the displacement of the fiber and the tensile matrix, respectively. We will assume small displacements throughout. Then, we may define the strain field in the fiber and tensile matrix respectively as

$$\begin{aligned} \varepsilon_f(z) &= \frac{dw_f}{dz}(z), \\ \varepsilon_{tm}(z) &= \frac{dw_{tm}}{dz}(z). \end{aligned} \tag{1}$$

Furthermore, the tensile matrix strain field may be separated into elastic and plastic parts,

$$\varepsilon_{tm}(z) = \varepsilon_{tm}^{\mathrm{el}}(z) + \varepsilon_{tm}^{\mathrm{pl}}(z), \tag{2}$$

and corresponding displacement fields defined as

$$\begin{aligned} w_{tm}^{\mathrm{el}}(z) &= \int_0^z \varepsilon_{tm}^{\mathrm{el}}(u)\, du, \\ w_{tm}^{\mathrm{pl}}(z) &= \int_0^z \varepsilon_{tm}^{\mathrm{pl}}(u)\, du. \end{aligned} \tag{3}$$

Since the fiber is assumed always elastic, such a decomposition is not carried out for its elastostatic fields. Another displacement field of interest is the slip displacement $w_x(z)$ which occurs at the interface between the fiber and the shear matrix. The slip displacement $w_x(z)$ is the relative displacement

in the between the fiber and the shear matrix at their interface as depicted schematically in Figure 2c.

Let $w_{sm}(r,z)$ be the displacement field in the shear matrix. Then, the shear strain field in the shear matrix $\gamma_{sm}(r,z)$ may be defined as

$$\gamma_{sm}(r,z) = \frac{\partial w_{sm}}{\partial r}(r,z). \tag{4}$$

We immediately note an important relation concerning $\gamma_{sm}(r,z)$:

$$\begin{aligned} \int_a^{\bar{R}} \gamma_{sm}(r,z)\, dr &= \int_a^{\bar{R}} \frac{\partial w_{sm}}{\partial r}(r,z)\, dr \\ &= w_{sm}(\bar{R},z) - w_{sm}(a,z) \\ &= w_{tm}(z) - w_f(z) - w_x(z) \end{aligned} \tag{5}$$

to be used in Sections 2.3 and 3.2 below. The last equality in Eq. (5) comes from assuming displacement continuity across the shear/tensile matrix interface, and the discontinuity to the extent w_x across the fiber/shear matrix interface as shown in Figure 2.

Obviously, all of these stress and displacement fields are also a function of the applied composite stress $\sigma_c = f_c/(\pi b^2)$ where f_c is the axial force applied to the composite. This dependence is however left to be tacitly assumed for the sake of notational brevity.

2.2 Constitutive Assumptions

The fiber is assumed to deform linear elastically following the one-dimensional Hooke's law:

$$\sigma_f(z) = E_f \varepsilon_f(z) \tag{6}$$

where E_f is the elastic stiffness of the fiber, and σ_f denotes the fiber stress. On the other hand, the uniaxial stress–strain (σ_u–ε_u) curve of the matrix in a tension test is approximated as consisting of a linear elastic part and a linear hardening part. That is,

$$\sigma_u = \begin{cases} E_1 \varepsilon_u, & \text{if } \sigma_u < \sigma_Y^{\mathrm{UA}}, \\ E_2 \varepsilon_u + (E_1 - E_2)\varepsilon_Y^{\mathrm{UA}}, & \text{if } \sigma_u \geq \sigma_Y^{\mathrm{UA}}, \end{cases} \tag{7}$$

where

$$\varepsilon_Y^{\mathrm{UA}} = \sigma_Y^{\mathrm{UA}} / E_1, \tag{8}$$

and σ_Y^{UA} is the matrix yield stress under uniaxial tension, E_1 the matrix elastic stiffness, and E_2 its hardening rate. Extending an idea of Prager (see Hill [14, pp 49]), Eq. (7) can be regularized as

$$\sigma_u = \sigma_Y^{\mathrm{UA}'} \tanh\left(\frac{(E_1 - E_2)\varepsilon_u}{\sigma_Y^{\mathrm{UA}'}}\right) + E_2 \varepsilon_u. \tag{9}$$

With

$$\sigma_Y^{\mathrm{UA}'} = \sigma_Y^{\mathrm{UA}} \left(1 - E_2/E_1\right), \tag{10}$$

the two branches of Eq. (7) are asymptotic limits of Eq. (9). The differentiability of Eq. (9), not available in the form Eq. (7) will prove valuable in the numerical solution of the governing equations in Section 2.4 by gradient methods.

Figure 3 shows the measured uniaxial stress-strain curve for bulk (monolithic) Al 6061 together with the two branches of Eq. (7) whose parameters E_1, E_2 and $\sigma_{Y,\,b}^{\mathrm{UA}}$ are appropriately fit. It is seen that the measured curve is well approximated by Eq. (7). As can also be seen, Eq. (9) is an even better approximation of the measured stress-strain curve. We emphasize that $\sigma_{Y,\,b}^{\mathrm{UA}}$ denotes the yield point of the monolithic matrix material, which in general will differ from the

yield point on the *in-situ* matrix material in uniaxial tension denoted by $\sigma_Y^{\rm UA}$. Typically, $\sigma_{Y,\,b}^{\rm UA} \leq \sigma_Y^{\rm UA}$ if the composite manufacturing process involves heat treatment which may yield and harden the matrix.

We next deduce the pure shear stress-strain (τ_u-γ_u) response from Eq. (7) using Nadai's deformation theory (see Budiansky [15]) for a matrix material point deforming under pure shear. According to Nadai's theory,

$$\varepsilon_u = \frac{\sigma_u}{E_s(\sigma_e)} \tag{11}$$

in uniaxial tension from which, comparing with Eq. (7) we find for the modulus E_s

$$E_s(\sigma_e) = \begin{cases} E_1, & \text{if } \sigma_e < \sigma_Y^{\rm UA} \\ \frac{\sigma_e E_1 E_2}{\sigma_e E_1 - \sigma_Y^{\rm UA}(E_1 - E_2)}, & \text{if } \sigma_e \geq \sigma_Y^{\rm UA}. \end{cases} \tag{12}$$

Here σ_e denotes the equivalent stress. $\sigma_e = \sigma_u$ in uniaxial tension. In a state of pure shear with shear stress τ_u, $\sigma_e = \sqrt{3}\tau_u$. Also, the yield point in the case of pure shear, $\tau_Y^{\rm UA}$ is related to the yield point in uniaxial tension, $\sigma_Y^{\rm UA}$ by the von Mises criterion as

$$\tau_Y^{\rm UA} = \sigma_Y^{\rm UA}/\sqrt{3}. \tag{13}$$

Now, Nadai's theory, specialized to the case of pure shear gives

$$\gamma_u = \frac{3}{2}\left(\frac{\tau_u}{E_s} - \frac{\tau_u}{E_1}\right) + \frac{\tau_u}{G_1} \tag{14}$$

where G_1 is the elastic shear modulus. Since $\sigma_e = \sqrt{3}\tau_u$ in the case of pure shear, this can be written using Eq. (12) as

$$\gamma_u = \begin{cases} \frac{\tau_u}{G_1}, & \text{if } \tau_u \leq \tau_Y^{\rm UA} \\ \frac{\tau_u}{G_2} - \tau_Y^{\rm UA}\left(\frac{1}{G_2} - \frac{1}{G_1}\right), & \text{if } \tau_u \geq \tau_Y^{\rm UA}, \end{cases} \tag{15}$$

where

$$\frac{1}{G_2} = \frac{1}{G_1} + \frac{3}{2}\left(\frac{1}{E_2} - \frac{1}{E_1}\right) \tag{16}$$

denotes the reciprocal hardening of the shear response. Inverting Eq. (15), we obtain in parallel with Eq. (7),

$$\tau_u = \begin{cases} G_1\gamma_u, & \text{if } \tau_u < \tau_Y^{\mathrm{UA}}, \\ G_2\gamma_u + (G_1 - G_2)\gamma_Y^{\mathrm{UA}}, & \text{if } \tau_u \geq \tau_Y^{\mathrm{UA}}, \end{cases} \tag{17}$$

where

$$\gamma_Y^{\mathrm{UA}} = \tau_Y^{\mathrm{UA}}/G_1. \tag{18}$$

Regularizing this expression exactly as before in Eq. (9), we have

$$\tau_u = \tau_Y^{\mathrm{UA}'} \tanh\left(\frac{(G_1 - G_2)}{\tau_Y^{\mathrm{UA}'}}\gamma_u\right) + G_2\gamma_u, \tag{19}$$

where $\tau_Y^{\mathrm{UA}'} = \tau_Y^{\mathrm{UA}}(1 - G_2/G_1)$.

We now turn from the uniaxial response of the matrix material either in pure tension, Eq. (9) or pure shear, Eq. (19) to its *in-situ* response in the composite. In the composite model of Figure 1a, even assuming only z-displacements everywhere, matrix material points deform in a combined state of tension and shear. If the tensile and shear stress at a certain fixed material point are $\hat{\sigma}$ and $\hat{\tau}$, then the equivalent stress at that point is given by $\sqrt{\hat{\sigma}^2 + 3\hat{\tau}^2}$. To similarly couple yielding in both the tensile and shear matrix at each cross-section of Figure 1b, we define the equivalent stress at a cross-section z as

$$\sigma_e(z) = \sqrt{\sigma_{tm}^2(z) + 3\tau_{sm}^2(\tilde{r}, z)}, \tag{20}$$

where $a < \tilde{r} \leq \bar{R}$ denotes a characteristic radial distance representative of the shear stress state in the shear matrix, and will be defined below in Eq. (44). $\sigma_{tm}(z)$ and $\tau_{sm}(r, z)$ denote the *in-situ* stress fields in the tensile and shear

matrices respectively. We then take the yield criterion for the cross-section z as

$$\sigma_e(z) = \sqrt{\sigma_{tm}^2(z) + 3\tau_{sm}^2(\tilde{r}, z)} = \sigma_Y^{\mathrm{UA}} = \sqrt{3}\tau_Y^{\mathrm{UA}}. \tag{21}$$

The value of $\sigma_{tm}(z)$ and $\tau_{sm}(\tilde{r}, z)$ which meet this criterion will be labeled as $\sigma_Y(z)$ and $\tau_Y(z)$. For use in the regularized constitutive laws, we also define

$$\begin{aligned} \sigma'_Y(z) &= \sigma_Y(z)(1 - E_2/E_1), \text{ and} \\ \tau'_Y(z) &= \tau_Y(z)(1 - G_2/G_1) \end{aligned} \tag{22}$$

With this adjustment for the yield point at each cross-section, we assume the *in-situ* response of the tensile and shear matrix material points to be identical in form to Eq. (9) and Eq. (19):

$$\sigma_{tm}(z) = \sigma'_Y(z) \tanh\left(\frac{(E_1 - E_2)\varepsilon_{tm}(z)}{\sigma'_Y(z)}\right) + E_2\varepsilon_{tm}(z), \tag{23}$$

and

$$\tau_{sm}(r, z) = \tau'_Y(z) \tanh\left(\frac{(G_1 - G_2)\gamma_{sm}(r, z)}{\tau'_Y(z)}\right) + G_2\gamma_{sm}(r, z). \tag{24}$$

Since it will prove convenient for algebraic manipulations later, we also record here the bilinear form of the approximation Eq. (24):

$$\tau_{sm}(r, z) = \begin{cases} G_1\gamma_{sm}(r, z), & \text{if } \tau_{sm} < \tau_Y(z), \\ G_2\gamma_{sm} + (1 - \frac{G_2}{G_1})\tau_Y(z), & \text{if } \tau_{sm} \geq \tau_Y(z). \end{cases} \tag{25}$$

$\sigma_Y(z)$ and $\tau_Y(z)$ must be calculated using an iterative incremental analysis, in each step of which the matrix yield zone and the stress field are adjusted until the yield condition $\sigma_e(z) \geq \sigma_Y^{\mathrm{UA}}$ is satisfied for z within the yield zone and not outside. For simplicity however, we follow the following approximate procedure for estimating them *a priori*. Suppose the stress field in the tensile and shear matrices for a linear elastic matrix and a perfect interface are known

to be $\sigma_p(z)$ and $\tau_p(r,z)$ respectively. We assume that

$$\frac{\sigma_Y(z)}{\tau_Y(\tilde{r},z)} = \frac{\sigma_p(z)}{\tau_p(\tilde{r},z)}, \tag{26}$$

i.e., the actual stress state at a cross-section on the verge of yielding is the same as it would be if the rest of the matrix were elastic and the interface perfectly bonded. Qualitatively speaking, the matrix constitutive assumptions made here will be valid so long as the composite loading is confined to a level such that the strain in every matrix material point is only a few times the yield strain, and the yielded length of the matrix is small (comparable to the fiber diameter). Precisely quantifying these limits will take a more detailed calculation, and is not done here.

Combining Eq. (26) and Eq. (21), we then have for each z,

$$\begin{aligned} \sigma_Y(z) &= \frac{\sigma_Y^{\mathrm{UA}}}{\sqrt{1+3(\tau_p(\tilde{r},z)/\sigma_p(z))^2}}, \text{ and} \\ \tau_Y(z) &= \frac{\sigma_Y^{\mathrm{UA}}}{\sqrt{3+(\sigma_p(z)/\tau_p(\tilde{r},z))^2}}. \end{aligned} \tag{27}$$

Eq. (23) and Eq. (24), together with Eq. (27) completely specify the constitutive law of the tension and shear matrices *in-situ* for each cross-section z provided the elastic fields σ_p and ε_p can be determined.

We next turn to a slipping criterion for the interface. A frequently used model assumes that the interface slips an indeterminate amount at a certain cross-section z if the shear stress exceeds a frictional threshold τ^* at that cross-section z, i.e.,

$$w_x(z) = \begin{cases} 0, & \text{if } \tau_i(z) < \tau^*, \\ c \ \mathrm{sign}(\tau_i(z)) & \text{if } \tau_i(z) = \tau^*, \end{cases} \tag{28}$$

where c is determined only to the extent that $c > 0$ and τ^* defines a frictional

slip threshold. In the present work, we use a regularized form of Eq. (28), viz.,

$$w_x(z) = w_{x0} \left| \frac{\tau_i(z)}{\tau^*} \right|^n \text{sign}(\tau_i(z)). \tag{29}$$

The exponent n determines the rapidity of the stick-to-slip transition. As seen in Figure 4 the constitutive law Eq. (29) approaches that expressed by Eq. (28) as $n \to \infty$ and is a good approximation for even $n = 30$. Choosing n much larger than this typically leads to difficulties associated with the floating point representation of numbers in computers. n is not a parameter of the present model; it should be chosen to be large enough so that Eq. (29) well approximates Eq. (28), but not so large as to cause floating point underflow problems. Also, for a fixed n, the model is unaffected by the individual values of w_{x0} and τ^* and only depends upon w_{x0}/τ^{*n}. Anticipating the order of magnitude of w_x in Section 4, we take $w_{x0} = 0.01$ mm and treat τ^* as the only parameter to facilitate explanation. Obviously, any arbitrary w_{x0} would do equally well and the corresponding τ^* would scale accordingly. The regularized Eq. (29), being differentiable for $|\tau_i(z)| > 0$, is amenable to a gradient-based numerical solution scheme for the governing equations below.

2.3 Governing Equations

The governing equations of the present problem consist of two differential equations: one expressing equilibrium of the fiber, and the other the equilibrium of each composite cross-section, and one algebraic equation expressing the slip condition Eq. (29). In formulating these, we ignore any pre-strains in the composite.

Based on the free body diagram for the fiber shown in Figure 1c, we write

the one-dimensional equilibrium condition for the fiber along the z-direction as follows:

$$\pi a^2 \frac{d\sigma_f}{dz}(z) + 2\pi a \tau_i(z) = 0, \tag{30}$$

where πa^2 is the fiber cross-sectional area, $2\pi a$ its circumference and $\tau_i(z)$ is the interfacial shear stress at coordinate z in the fiber direction. Simplifying, we get

$$\frac{d\sigma_f}{dz}(z) + \frac{2}{a}\tau_i(z) = 0. \tag{31}$$

Since tensile *force* must be conserved in every z cross-section, and the shear matrix transmits no tension, we have

$$\frac{d}{dz}[\pi a^2 \sigma_f(z) + \pi(b^2 - a^2)\sigma_{tm}(z)] = 0, \tag{32}$$

or,

$$\frac{d\sigma_f}{dz}(z) + \frac{b^2 - a^2}{a^2}\frac{d\sigma_{tm}}{dz}(z) = 0. \tag{33}$$

Here, $\pi(b^2 - a^2)$ is the cross-sectional area of the matrix (Figure 1a).

We next express the equilibrium equations Eq. (31) and Eq. (33) in terms of the displacements fields $w_f(z)$, $w_{tm}(z)$ and $w_x(z)$ using the constitutive assumptions for the fiber and matrix materials. For the fiber, we readily have $\sigma_f = E_f dw_f/dz$ from Eq. (6). Thus,

$$\frac{d\sigma_f}{dz} = E_f \frac{d^2 w_f}{dz^2}. \tag{34}$$

Differentiating the constitutive law Eq. (23) for the tensile matrix, and using Eq. (1), we also have

$$\frac{d\sigma_{tm}}{dz}(z) = \left(\operatorname{sech}^2\left(\frac{E_1 - E_2}{\sigma_Y'(z)}\frac{dw_{tm}}{dz}(z)\right)(E_1 - E_2) + E_2\right)\frac{d^2 w_{tm}}{dz^2}(z). \tag{35}$$

The representation of $\tau_i(z)$ in terms of the displacement fields is somewhat

more involved. Solving the equilibrium equation of the shear matrix,

$$\frac{\partial \tau_{sm}}{\partial r}(r,z) + \frac{\tau_{sm}(r,z)}{r} = 0 \tag{36}$$

with the interfacial boundary condition $\tau(r=a,z) = \tau_i(z)$, we obtain

$$\tau_{sm}(r,z) = \frac{a\tau_i(z)}{r}. \tag{37}$$

From Eq. (25), we have for the constitutive equation of material points in the shear matrix,

$$\tau_{sm}(r,z) = \frac{a\tau_i(z)}{r} = \begin{cases} G_1\gamma_m(r,z), & \text{if } \tau_{sm}(\tilde{r},z) \le \tau_Y(z) \\ G_2\gamma_m(r,z) + \frac{G_1-G_2}{G_1}\tau_Y(z), & \text{if } \tau_{sm}(\tilde{r},z) \ge \tau_Y(z). \end{cases} \tag{38}$$

Integrating both sides from $r=a$ to $\bar{R}$, and using Eq. (5), we obtain

$$a\tau_i(z)\log\left(\frac{\bar{R}}{a}\right) = \begin{cases} G_1(w_{tm}(z) - w_f(z) - w_x(z)), & \text{if } \tau_{sm}(\tilde{r},z) \le \tau_Y(z), \\ G_2(w_{tm}(z) - w_f(z) - w_x(z)) & \\ \quad + \frac{G_1-G_2}{G_1}\tau_Y(z)(\bar{R}-a), & \text{if } \tau_{sm}(\tilde{r},z) \ge \tau_Y(z). \end{cases} \tag{39}$$

Suppose z^* is such that $\tau_{sm}(\tilde{r},z^*) = \tau_Y(z^*)$, i.e.,

$$\frac{a\tau_i(z^*)}{\tilde{r}} = \tau_Y(z^*) \tag{40}$$

and the switch occurs from one branch to the other in Eq. (39) at $z=z^*$. $z=z^*$ thus is the axial location of the boundary between the plastic and elastic regions of the matrix. Now, τ_i must be a continuous function of z for equilibrium of the shear matrix at $z=z^*$. This implies the continuity of the right side branches of Eq. (39), i.e.,

$$w_{tm}(z^*) - w_f(z^*) - w_x(z^*) = \tau_Y(z^*)(\bar{R}-a)/G_1 \tag{41}$$

Condition Eq. (41), together with the equality with first of the branches of Eq. (39)

$$a\tau_i(z^*)\log(\bar{R}/a)/G_1 = w_{tm}(z^*) - w_f(z^*) - w_x(z^*) \tag{42}$$

implies

$$\tau_i(z^*) = \frac{\tau_Y(\bar{R}-a)}{a\log(\bar{R}/a)}. \tag{43}$$

Comparing Eq. (43) and Eq. (40), we find

$$\tilde{r} = \frac{\bar{R}-a}{\log(\bar{R}/a)}. \tag{44}$$

It is easily verified that $a \leq \tilde{r} \leq \bar{R}$. Setting $\tilde{r}$ according to Eq. (44) thus ensures continuity of the right side of Eq. (39) at the boundary $z = z^*$ between the yielded and elastic cross-sections of the matrix defined according to Eq. (21). We may now rewrite Eq. (39) as

$$\tau_i(z) = \begin{cases} \frac{G_1}{a\log(\bar{R}/a)}(w_{tm}(z) - w_f(z) - w_x(z)), & \tau_i(z) \leq \frac{\tau_Y(z)(\bar{R}-a)}{a\log(\bar{R}/a)}, \\ \frac{G_2}{a\log(\bar{R}/a)}(w_{tm}(z) - w_f(z) - w_x(z)) & \\ \quad + \frac{G_1-G_2}{G_1}\frac{\tau_Y(z)(\bar{R}-a)}{a\log(\bar{R}/a)}, & \tau_i(z) \geq \frac{\tau_Y(z)(\bar{R}-a)}{a\log(\bar{R}/a)}. \end{cases} \tag{45}$$

Regularizing this expression along the same lines as Eq. (9), we finally obtain

$$\begin{aligned} \tau_i(z) = {} & \frac{\tau_Y'(z)(\bar{R}-a)}{a\log(\bar{R}/a)}\tanh\left[\frac{G_1-G_2}{\tau_Y'(z)(\bar{R}-a)}(w_{tm}(z) - w_f(z) - w_x(z))\right] \\ & + \frac{G_2}{a\log(\bar{R}/a)}\left[w_{tm}(z) - w_f(z) - w_x(z)\right]. \end{aligned} \tag{46}$$

Thus, we have expressed all the terms in the equilibrium equations Eq. (31) and Eq. (33) in terms of displacement fields. Resubstituting, we can write a pair of governing differential equations:

$$\begin{aligned} & E_f\frac{d^2w_f}{dz^2}(z) + \frac{2\tau_Y'(\bar{R}-a)}{a^2\log(\bar{R}/a)}\tanh\left[\frac{G_1-G_2}{\tau_Y'(\bar{R}-a)}(w_{tm}(z) - w_f(z) - w_x(z))\right] \\ & \qquad \frac{2G_2}{a^2\log(\bar{R}/a)}\left[w_{tm} - w_f - w_x\right] = 0 \end{aligned} \tag{47}$$

obtained using Eq. (46) and Eq. (31), and

$$E_f \frac{d^2 w_f}{dz^2} + \frac{b^2 - a^2}{a^2} \frac{d^2 w_{tm}}{dz^2}(z) \times \left[\operatorname{sech}^2 \left(\frac{E_1 - E_2}{\sigma_Y'(z)} \frac{dw_{tm}(z)}{dz} \right) (E_1 - E_2) + E_2 \right] = 0 \tag{48}$$

obtained using Eq. (35) and Eq. (33). The slip constitutive equation Eq. (29) supplies an algebraic governing equation:

$$\frac{w_{x0}}{\tau^* a \log(\bar{R}/a)} \left| \tau_Y'(\bar{R} - a) \tanh \left(\frac{G_1 - G_2}{\tau_Y'(\bar{R} - a)} (w_{tm} - w_f - w_x) \right) + G_2 (w_{tm} - w_f - w_x) \right|^n \operatorname{sign}(\tau_i(z)) - w_x(z) = 0 \tag{49}$$

upon substituting $\tau_i(z)$ from Eq. (46). The three governing equations Eqs. (47) – (49) in three variables $w_{tm}(z)$, $w_f(z)$, and $w_x(z)$ must be solved subject to the following four boundary conditions:

$$\begin{cases} \frac{dw_f}{dz}(z = 0) = 0 & \text{if the fiber is broken,} \\ w_f(z = 0) = 0 & \text{if the fiber is intact,} \end{cases} \tag{50}$$

$$\frac{dw_{tm}}{dz}(z = \ell) = \begin{cases} \frac{b^2}{b^2 - a^2} \frac{\sigma_c}{E_1}, & \frac{b^2 \sigma_c}{b^2 - a^2} \leq \sigma_Y(\ell), \\ \frac{b^2}{b^2 - a^2} \frac{\sigma_c}{E_2} - \left(\frac{1}{E_2} - \frac{1}{E_1} \right) \sigma_Y(\ell), & \frac{b^2 \sigma_c}{b^2 - a^2} \geq \sigma_Y(\ell), \end{cases} \tag{51}$$

$$w_{tm}(z = 0) = 0, \tag{52}$$

and

$$\frac{dw_f}{dz}(z = \ell) = 0. \tag{53}$$

Note that the loading boundary condition Eq. (51) prescribes the strain in the matrix at $z = \ell$ with reference to stress $\sigma_c b^2/(b^2 - a^2)$ which is the local stress in the matrix assuming all the load is applied to it uniformly. Note also the matrix strain is prescribed depending on whether or not the tensile matrix has yielded at $z = \ell$.

The two differential equations Eq. (47), Eq. (48) and the one algebraic governing equation Eq. (49) are non-linear and a full analytical solution for them subject to the boundary conditions Eq. (50) — Eq. (53) is not possible. The numerical shooting method (Roberts and Shipman [16]) becomes unstable when the matrix yields and is therefore unsuited for their solution. The finite difference method (Collatz [17]) however does not suffer this deficiency, and is used here. Following this method, we replace the non-linear differential equations with non-linear algebraic equations by approximating the differential coefficients using the lowest order central differences, which are then solved. We discretize the domain of the problem $0 \leq z \leq \ell$ using nodes $z^{(\iota)} = \iota h$, $\iota = 0, 1, 2, \ldots, N$. We also form two "boundary nodes" at $z^{(\iota=-1)} = -h$, and $z^{(\iota=N+1)} = \ell + h$. Denoting the function values of $w_f(z)$, $w_{tm}(z)$, and $w_x(z)$ at $z = z^{(\iota)}$ also with the superscript (ι), the approximate form of Eq. (47) can be written as

$$\begin{aligned} & w_f^{(\iota+1)} - 2w_f^{(\iota)} + w_f^{(\iota-1)} + \\ & \quad \frac{2h^2\tau_Y'(\bar{R}-a)}{E_f a^2 \log(\bar{R}/a)} \tanh\left(\frac{G_1 - G_2}{\tau_Y'(\bar{R}-a)}(w_{tm}^{(\iota)} - w_f^{(\iota)} - w_x^{(\iota)})\right) \\ & \quad \frac{2G_2 h^2}{E_f a^2 \log(\bar{R}/a)}\left(w_{tm}^{(\iota)} - w_f^{(\iota)} - w_x^{(\iota)}\right) = 0. \end{aligned} \tag{54}$$

This approximation will improve with decreasing h. Similarly, Eq. (48) is approximately

$$\begin{aligned} & w_f^{(\iota+1)} - 2w_f^{(\iota)} + w_f^{(\iota-1)} + \frac{(b^2-a^2)}{E_f a^2}(w_{tm}^{(\iota+1)} - 2w_{tm}^{(\iota)} + w_{tm}^{(\iota-1)}) \times \\ & \quad \left\{(E_1 - E_2)\mathrm{sech}^2\left(\frac{E_1 - E_2}{\sigma_Y'}\frac{w_{tm}^{(\iota+1)} - w_{tm}^{(\iota-1)}}{2h}\right) + E_2\right\} = 0 \end{aligned} \tag{55}$$

and Eq. (49)

$$\frac{w_{x0}}{\tau^* a \log(\bar{R}/a)} \left| \tau_Y'(\bar{R}-a) \tanh\left(\frac{G_1 - G_2}{\tau_Y'(\bar{R}-a)} (w_{tm}^{(\iota)} - w_f^{(\iota)} - w_x^{(\iota)}) \right) + G_2 (w_{tm}^{(\iota)} - w_f^{(\iota)} - w_x^{(\iota)}) \right|^n \operatorname{sign}(\tau_i(z)) - w_x^{(\iota)} = 0. \tag{56}$$

The finite difference equations Eqs. (54), (55), and (56) apply for $\iota = 0, \ldots, N$, i.e., do not apply at the boundary nodes and thus represent $3N+3$ equations.

The four boundary conditions Eqs. (50) – (53) can also be expressed in difference form using the boundary nodes:

$$\begin{cases} w_f^{(1)} - w_f^{(-1)} = 0 & \text{if the fiber is broken,} \\ w_f^{(0)} = 0 & \text{if the fiber is intact,} \end{cases} \tag{57}$$

$$\frac{w_{tm}^{(N+1)} - w_{tm}^{(N-1)}}{2h} = \begin{cases} \frac{b^2}{b^2-a^2} \frac{\sigma_c}{E_1}, & \frac{b^2 \sigma_c}{b^2-a^2} \le \sigma_Y(\ell), \\ \frac{b^2}{b^2-a^2} \frac{\sigma_c}{E_2} - \left(\frac{1}{E_2} - \frac{1}{E_1} \right) \sigma_Y(\ell), & \frac{b^2 \sigma_c}{b^2-a^2} \ge \sigma_Y(\ell), \end{cases} \tag{58}$$

$$w_{tm}^{(0)} = 0, \tag{59}$$

and

$$w_f^{(N+1)} - w_f^{(N-1)} = 0 \tag{60}$$

The $3N+7$ non-linear equations are then solved for as many unknowns: $w_f^{(\iota)}$, $w_{tm}^{(\iota)}$, $\iota = -1, \ldots, N+1$, and $w_x^{(\iota)}$, $\iota = 0, \ldots, N$ using the Newton-Raphson iterative procedure which sets up a banded linear system for solution. We calculate the displacement solution in applied stress increments / decrements of $\Delta\sigma_c = \pm 1$ MPa, and use the solution obtained at a certain σ_c as the initial guess for the Newton-Raphson scheme at $\sigma_c + \Delta\sigma_c$. We pick the rule of mixtures solution [1] as the initial guess for $\sigma_c = 1$ MPa.

3 Shear-Lag Model of Unloading

We now consider the evolution of stresses and displacements in the composite as it is unloaded monotonically from the maximum stress during the loading half cycle, $\sigma_c = \sigma_c^{\max}$.

3.1 Assumptions

The geometric and kinematic assumptions of Section 2.1 still apply in the unloading model. As in the loading model, the fiber is assumed to deform linear elastically. However, both the tensile and shear matrices are assumed to deform linear elastically as well. That is, the equivalent stress which each matrix material point faces during unloading is assumed to lie inside its yield envelope formed after loading, with strain hardening. Thus,

$$\begin{aligned} \sigma_{tm} &= E_1(\varepsilon_{tm} - \varepsilon_{tm}^{\mathrm{pl}}), \text{ and,} \\ \tau_{sm} &= G_1(\gamma_{sm} - \gamma_{sm}^{\mathrm{pl}}), \end{aligned} \tag{61}$$

where $\varepsilon_{tm}^{\mathrm{pl}}$ and $\gamma_{sm}^{\mathrm{pl}}$ denote, respectively the plastic set at a tensile and shear matrix material point. Both parts of the matrix are assumed not to yield in reverse, so that the plastic set in each part remains constant during unloading. Thus $\varepsilon_{tm}^{\mathrm{pl}}(z)$ and, by Eq. (3) $w_{tm}^{\mathrm{pl}}(z)$ remain constant in the tensile matrix. In particular, if $\sigma_{tm}^{\max}(z)$ and $\varepsilon_{tm}^{\max}(z)$ denote the stress and strain fields in the tensile matrix when $\sigma_c = \sigma_c^{\max}$, then

$$\varepsilon_{tm}^{\mathrm{pl}}(z) = \varepsilon_{tm}^{\max}(z) - \frac{\sigma_{tm}^{\max}(z)}{E_1}. \tag{62}$$

As in the loading model (see text after Eq. (5)) the calculation of $\gamma_{sm}^{\mathrm{pl}}(r,z)$ will be unnecessary in the shear-lag model; only $\int_a^{\bar{R}} \gamma_{sm}^{\mathrm{pl}}(r,z)\, dr$ will be needed,

which we will deduce indirectly in Section 3.2 below.

3.2 Governing Equations

The differential equations expressing equilibrium of the fiber, tensile matrix, and shear matrix, Eqs. (31,33,36) remain applicable during unloading since they do not depend upon the material constitutive law. Following the development of Eq. (38)–Eq. (46), we now express $\tau_i(z)$ during unloading in terms of the solution displacement fields. From Eq. (61), we have

$$\tau_{sm}(r,z) = \frac{a\tau_i(z)}{r} = G_1(\gamma_{sm}(r,z) - \gamma_{sm}^{\rm pl}(r,z)). \tag{63}$$

Integrating both sides from $r = a$ to $r = \bar{R}$, and using Eqs. (5) and (3),

$$a\tau_i \log\left(\frac{\bar{R}}{a}\right) = G_1(w_{tm}^{\rm el} + w_{tm}^{\rm pl} - w_f - w_x) - G_1 \int_a^{\bar{R}} \gamma_{sm}^{\rm pl}\, dr. \tag{64}$$

Now, defining the shear matrix plastic displacement as

$$w_{sm}^{\rm pl}(z) = -\int_a^{\bar{R}} \gamma_{sm}^{\rm pl}\, dr, \tag{65}$$

we may write

$$\tau_i = \frac{G_1}{a\log(\bar{R}/a)}(w_{tm}^{\rm el} + w_{tm}^{\rm pl} - w_f - w_x + w_{sm}^{\rm pl}). \tag{66}$$

This implies that $\tau_i = 0$, when $w_{tm}^{\rm el} + w_{tm}^{\rm pl} - w_f - w_x = -w_{sm}^{\rm pl}$, i.e., the relaxed state of the shear matrix corresponds to a relatively displaced fiber and tensile matrix. $w_{sm}^{\rm pl}$ thus quantifies the plastic displacement of the shear matrix.

As the applied stress is lowered from $\sigma_c = \sigma_c^{\max}$, we expect continuous variation (with σ_c) of stress fields $\sigma_f(z)$, $\sigma_{tm}(z)$, and $\tau_{sm}(z)$, for each z. By Eqs. (31) and (33), this continuity follows if the interfacial shear stress, $\tau_i(z)$ varies

continuously with the applied stress σ_c, for all $0 \leq z \leq \ell$. The continuity of the interfacial shear stress field $\tau_i(z)$ with applied load at $\sigma_c = \sigma_c^{\max}$ furnishes a criterion to determine $w_{sm}^{\rm pl}(z)$ which remains constant during the unloading half-cycle. Equating the expressions of Eq. (46) and Eq. (66), when $\sigma_c = \sigma_c^{\max}$ we get

$$\begin{aligned} \frac{\tau_Y'(\bar{R}-a)}{a\log(\bar{R}/a)}\tanh\left(\frac{G_1-G_2}{\tau_Y'(\bar{R}-a)}(w_{tm}-w_f-w_x)\right)+ \\ \frac{G_2}{a\log(\bar{R}/a)}\left(w_{tm}-w_f-w_x\right)= \\ \frac{G_1}{a\log(\bar{R}/a)}\left(w_{tm}-w_f-w_x+w_{sm}^{\rm pl}\right), \end{aligned} \tag{67}$$

or,

$$\begin{aligned} w_{sm}^{\rm pl}(z) = \left(\frac{G_2}{G_1}-1\right)\left(w_{tm}(z)-w_f(z)-w_x(z)\right)+ \\ \frac{\tau_Y(\bar{R}-a)}{G_1}\tanh\left(\frac{G_1-G_2}{\tau_Y(\bar{R}-a)}(w_{tm}(z)-w_f(z)-w_x(z))\right). \end{aligned} \tag{68}$$

Fiber equilibrium Eq. (31) together with Eq. (66) gives one governing equation during unloading

$$E_f\frac{d^2w_f}{dz^2}+\frac{2G_1}{a^2\log(\bar{R}/a)}(w_{tm}^{\rm el}+w_{tm}^{\rm pl}-w_f-w_x+w_{sm}^{\rm pl})=0 \tag{69}$$

while the consideration of cross-sectional equilibrium Eq. (33) gives another

$$E_f\frac{d^2w_f}{dz^2}+E_1\frac{b^2-a^2}{a^2}\frac{d^2w_{tm}^{\rm el}}{dz^2}=0. \tag{70}$$

In writing the second term, we have used Eqs. (61), (2), and (3). As during loading, a third algebraic governing equation is obtained from the assumed slip constitutive equation Eq. (28) as

$$w_{x0}\left|\frac{G_1}{\tau^* a\log(\bar{R}/a)}(w_{tm}^{\rm el}+w_{tm}^{\rm pl}-w_f-w_x+w_{sm}^{\rm pl})\right|^n \operatorname{sign}(\tau_i(z))-w_x(z)=0. \tag{71}$$

The solution $w_f(z)$, $w_{tm}^{\rm el}(z)$, and $w_x(z)$ for this set of governing equations

must be determined subject to boundary conditions which are identical to those during the loading half-cycle, except that the loading boundary condition Eq. (51) must now be replaced with

$$\frac{dw_{tm}^{\mathrm{el}}}{dz}(z=\ell) = \frac{b^2}{b^2-a^2}\frac{\sigma_c}{E_1}, \tag{72}$$

since the matrix is always assumed linear elastic. Numerical solution using the finite difference method of this set of equations follows the same general scheme as during loading (Section 2.4), and will not be detailed here.

4 Experimental Verification

As stated at the outset, the present model is motivated by an experiment by Hanan *et al* [1]. Before comparing their measurements to the predictions of the present model, we pause to summarize the relevant aspects of their experiment. Hanan *et al*'s experiment consisted of cyclic tensile loading of an alumina fiber/aluminum matrix composite with a single embedded fiber. The stress-strain response of the monolithic matrix material is shown in Figure 3. The specimen was manufactured by casting the aluminum 6061 alloy around a notched fiber to assure its fracture upon loading. It was considered likely that the *in-situ* properties of the matrix, especially its yield stress, may have changed during specimen manufacture. An X-ray radiograph taken at the end of load cycling revealed that the fiber did indeed fracture although the fracture load could not be experimentally determined. The specimen ends were screwed into the testing machine, i.e., all the load was applied to the matrix. During the first cycle of loading at room temperature, the composite was tensioned to $\sigma_c^{(1)} = 80$ MPa. The second and later load cycles consisted

of loading to $\sigma_c^{(2)} = 100$ MPa and unloading back to $\sigma_c = 0$ MPa. At load intervals of 20 MPa or smaller during these cycles, the load was held fixed for about an hour, and the *elastic axial* strain in the fiber and matrix were separately measured using neutron diffraction. Hanan *et al* observe that the residual strain in the fiber is tensile and that in the matrix is compressive after each of the cycles. They qualitatively reason this to arise from matrix plastic deformation during loading. For compatible deformation between fiber and matrix during the subsequent unloading, they reason that the fiber must counteract some of the matrix plastic strain by compressing it elastically, while the fiber tensile strain itself arises as the reaction to this action. The present model lends quantitative form and detail to this qualitative argument.

It is important to note that the axial strain measured in each phase was a volume average over the neutron gage volume depicted in Figure 5. In order to compare the model predictions with the measured strain, we must therefore average the axial strain field $\varepsilon_{tm}^{\mathrm{el}}(z)$ calculated by the model over the neutron gage volume. For this purpose we develop the calculated one-dimensional fields $\varepsilon_f(z)$, and $\varepsilon_{tm}^{\mathrm{el}}(z)$ into axisymmetric fields $\epsilon_f(r,z) = \varepsilon_f(z)$, $0 \leq r \leq a$, and $\epsilon_{tm}^{\mathrm{el}}(r,z) = \varepsilon_{tm}^{\mathrm{el}}(z)$, $a \leq r \leq b$. We then average the fields ϵ_f and ϵ_{tm} over the volume of the fiber and the matrix probed by the neutron beam to obtain $\bar{\epsilon}_f$ and $\bar{\epsilon}_{tm}^{\mathrm{el}}$, repsectively. Also, since it is unknown experimentally when the fiber failed, in the model we assume the fiber fractured prior to any loading at $z = 0$ mm. This assumption will be borne out shortly by the predictions it yields. Also, since the present model does not account for residual strains from previous cycles (although it does calculate residual strains at the end of each cycle), we model cycle 2 as loading the composite directly to $\sigma_c = 100$ MPa. We expect the model load path to reasonably follow the experimental

one in the range $\sigma_c^{(1)} \leq \sigma_c \leq \sigma_c^{(2)}$ during the loading half of cycle 2 and throughout the subsequent unloading, provided interfacial slip was limited during cycle 1 unloading. We do not model cycles 3 and above because the predicted evolution of all stress and displacement fields during these cycles will trivially coincide with those of cycle 2 as residual strains are ignored by the model. While the experimental data shows evolution of strains between cycle 2 and cycle 3, cycle 4 onward retrace the same strain evolution as cycle 3 with loading.

Figure 6 compares the measured average axial strain evolution in the fiber and matrix during cycle 1 with those calculated using the present model. Two scalar parameters: the *in-situ* yield point σ_Y^{UA} (different from $\sigma_{Y,b}^{\mathrm{UA}}$ in Figure 3; see text below Eq. (10)), and the frictional threshold of the interface τ^*, are fit so as to obtain these comparisons. Their values, together with those of other constants of the model are listed in Table 1. As can be seen, the *in-situ* yield point of the matrix seems to have increased from its bulk value of 93 MPa to 108 MPa.

The success of the model in capturing the measured strain evolution in cycle 1 with these parameters suggests that despite the numerous simplifying geometric and constitutive assumptions made, the errors committed in approximating the elastic strain field in the present one-dimensional model average out over the neutron gage volume. This, and a similar observation to be made regarding cycle 2 below, *a posteriori* justify the use of the shear-lag approach in modeling the stress field in a damaged metal matrix composite.

Several observations follow from the model-data comparisons in Figure 6 for cycle 1. The excellent agreement of the model predictions at small σ_c with

those experimentally observed suggests that in the specimen, the fiber fractured at the notch either during specimen manufacture, or at a very small load (say $\sigma_c \leq 5$ MPa) during cycle 1. As σ_c is increased to about 35 MPa, the model predictions for both fiber and matrix strain evolutions show qualitatively different behavior which signals the onset of matrix yielding. It arises because of the increased compliance of the matrix due to plasticity, which transfers more of the applied axial stress to the fiber. This transition is missed by the experiment on account of its large load step size between strain measurements. The agreement of the predicted and measured strains deteriorates somewhat with increasing load. At $\sigma_c = 80$ MPa, the model overpredicts both $\bar{\epsilon}_f$ (measured: 350×10^{-6}, calculated: 410×10^{-6}) and $\bar{\epsilon}^{\rm el}_{lm}$ (measured: 590×10^{-6}, calculated: 740×10^{-6}). If the model were erring in the magnitude of load transfer from the matrix to the fiber through interfacial shear, it would underpredict one of these while overpredicting the other. The observed discrepancy must therefore be due to the discrepancy between the actual and calculated interfacial shear profiles. During unloading the model accurately reproduces the slope of the unloading curves near $\sigma_c = 0$ MPa, while overestimating the fiber residual strain (measured: 170×10^{-6}, calculated: 200×10^{-6}) and underestimating that in the matrix (measured: -380×10^{-6}, calculated: -470×10^{-6}) unlike the situation at the peak load. This suggests that the model may not be calculating the actual load transfer from matrix to fiber correctly in this case. The model is also unable to capture the kink – the curious decrease and followed by a slight increase in fiber strain – at $\sigma_c = 40$ MPa and 20 MPa during unloading.

The deterioration of the model at higher σ_c, and the kink may have several causes among which we are unable to discriminate with the available information. We however strongly suspect the following two possibilities: (i) A

gradual breakdown of the assumed constitutive laws with increasing loading. This may take the form of increasing inapplicability of the frictional criterion Eq. (29) at the interface, especially since the model calculates a sizable increase in the slip displacement between $\sigma_c = 60$ and 80 MPa during loading ($w_x(z = 0, \sigma_c = 60\text{MPa}) = -0.008$ mm, $w_x(z = 0, \sigma_c = 80\text{MPa}) = -0.023$ mm). Also, the constitutive assumption Eq. (26) which led to the *a priori* determined form for the tensile and shear matrix constitutive laws may be increasingly violated at larger σ_c. (ii) A peculiarity of the interface in this particular specimen. In reality, we expect the frictional threshold of the interface τ^* to show statistical variation along the interface. If large, this variation can cause the observed kinks in the measured elastic strain response by significantly perturbing the interfacial shear field. The extent and significance of this variability can only be known by repeating the experiment with nominally identical specimens and studying the scatter in the measured strains. Scatter comparable to the observed kink in this experiment would support the hypothesis that the kinks arise from this variability.

As stated already, the incapacity of the model to accommodate residual strains necessitates that we model cycle 2 as loading starting from a strain-free composite to $\sigma_c^{(2)} = 100$ MPa. In comparing the calculated and measured strains during cycle 2 shown in Figure 7, we must therefore only compare the part of the loading curve between $\sigma_c = 80$ and 100 MPa, and the entire unloading curve. With the constants of the model the same as those used in predicting cycle 1, as listed in Table 1, the model predicts very accurately the peak strain at $\sigma_c = 100$ MPa (measured: 430×10^{-6}, calculated: 450×10^{-6}) and residual strain (measured: 290×10^{-6}, calculated: 290×10^{-6}) in the fiber and also the residual matrix strain (measured: -630×10^{-6}, calculated: -650×10^{-6}). The

model peak stress however overestimates the peak matrix strain (measured: 900×10^{-6}, calculated: 1060×10^{-6}). Although capturing the peak and residual strain values the model and the experiment do not coincide even qualitatively in the interim. Indeed, the experimental data shows many kinks: Upon unloading from the peak load, the measured fiber strain is lower than its value during loading at the same σ_c until about $\sigma_c = 40$ MPa at which point it abruptly starts to increase until $\sigma_c = 10$ MPa and thereafter decreases. In contradistinction, the model predicts a monotonic decrease in fiber strains upon unloading whose values always exceed the corresponding fiber strain value during loading. The observed non-monotonicity in the experimental data lends further support to our suggestion above that the actual interfacial frictional threshold is much more complicated than the constant function τ^* assumed and local stick-slip processes are affecting the strain measurements.

Figure 7 also gives a sense of the sensitivity of the model to the parameters τ^* and σ_Y^{UA} by plotting the peak and residual strains in cycle 2 calculated with slightly perturbed parameters. The peak and residual strains hardly change when σ_Y^{UA} is increased from 108 to 118 MPa, keeping all other parameters as in Table 1. Although not shown, this perturbation postpones the widespread matrix yielding hitherto at $\sigma_c = 35$ MPa, to about $\sigma_c = 38$ MPa. The model however is more sensitive to τ^* which governs the load transfer from matrix to fiber. When increased from 51 to 56 MPa, keeping all other parameters as in Table 1, the peak fiber strain increases by 23×10^{-6}, while that in the matrix decreases by 50×10^{-6}. We caution against deducing from this observation that $\tau^* = 56$ MPa represents a better parametric value than $\tau^* = 51$ MPa since it misses the measured peak strain in the fiber less than the improvement it brings to the matrix strain. For, due to the large fiber-matrix stiffness ratio,

the discrepancy of 23×10^{-6} corresponds to a much larger error in fiber stresses, than the 50×10^{-6} improvement does in the matrix. The residual strains are still quite insensitive to this perturbation.

We may thus be justified in claiming that statistical variations from specimen to specimen apart, the present model is a good representation of the average behavior among nominally identical single fiber alumina/aluminum composite specimens. Given this, the stress and displacement fields predicted by the model may be regarded as representative of the actual fields in the experimental specimen. We therefore plot these calculated fields at the two most interesting stages of the experiment in cycle 2: (i) At the peak load $\sigma_c = 100$ MPa, in Figures 8 and 9 and (ii) after unloading to $\sigma_c = 0$ MPa from the peak load, in Figures 10 and 11.

Figure 8 shows the calculated stress field in the fiber, tensile matrix and interface at $\sigma_c = 100$ MPa. In keeping with the boundary conditions of the model, the fiber ($\sigma_f(z)$) and matrix ($\sigma_{tm}(z)$) axial stress fields are symmetric about $z = \ell/2$, while the interfacial shear stress field is anti-symmetric about this point; in particular $\tau_i(\ell/2) = 0$. The roundedness of the fiber stress profile seen in this figure suggests incomplete load transfer from the matrix to the fiber. If repeated with a sufficiently long composite load transfer from the matrix to the fiber may be complete, and the slope $d\sigma_f/dz(z = \ell/2)$ will approach zero. The saturation of $\tau_i(z)$ near both traction free ends of the fiber at $z = 0$ and $z = \ell$ is also seen and indicates slipping in these regions.

Figure 10, which corresponds to the unloaded condition of the composite is more complicated than Figure 8 since the residual fields here are a product of competition between elastic recovery on the one hand and plastic deformation

and slip on the other. The observed profiles are qualitatively best understood by beginning with $\tau_i(z)$. As seen, near $z = 0$ and $z = \ell$, the interfacial shear stress remains unchanged from the stress state at the peak load. This is because compatible deformation between the elastic fiber and the matrix with a large plastic deformation is being imposed by compressing the matrix and tensioning the fiber elastically. The shear stresses thus imposed near $z = 0$ and $z = \ell$ set up a strain field which causes incompatibility at about 3.5 mm from each end, and to enforce compatibility there, a balancing shear stress of the opposite sense is needed. This stress induces slight reverse slip. As can be seen, the end result of the complex stress-transfer across the interface is that matrix is almost entirely in compression and the fiber in tension at $\sigma_c = 0$.

Figures 9 and 11 show respectively the calculated displacement field in the composite at $\sigma_c = 100$ MPa, and after unloading to $\sigma_c = 0$ MPa. As can be seen in both figures, $w_{tm}^{\rm pl}$ far exceeds the elastic part $w_{tm}^{\rm el}$, and near the middle (e.g., 6.5 mm $\leq z \leq$ 12.5 mm) the tensile matrix displacement almost coincides with that of the fiber (does so exactly at $z = \ell/2$). When $\sigma_c = 100$ MPa, we observe a crack opening displacement of about 0.048 mm, which is not much diminished upon unloading (0.039 mm). The key difference between the two cases is that the matrix is in compression at $\sigma_c = 0$, as opposed to the case at $\sigma_c = 100$ MPa when it is in tension.

Finally, as stated below Eq. (29), in fitting the parameters of the model we arbitrarily assumed $w_{x0} = 0.01$ mm and obtained $\tau^* = 51$ MPa as the best fit value. From Figures 9 and 11, we see that the actual slip displacements are indeed of the order of $w_{x0} = 0.01$ mm. The physical meaning of τ^* is directly seen from Eq. (29): τ^* represents the interfacial shear stress needed to cause a slip displacement of $w_{x0} = 0.01$ mm. It can also be readily seen that $\tau^* = 51$

MPa is approximately the saturation value of $\tau_i(z)$ in Figures 8 and 10.

5 Conclusions

By accounting for matrix elasto-plasticity and interfacial slip in a metal-matrix composite, the present shear lag model succeeds quite well in reproducing the measured strain evolution with applied stress in both phases of an Al_2O_3/Al composite. The model is successful in capturing the general trend of the measured strain evolution while being incapable of capturing the kinks (far larger than experimental error bars) observed in the strain measurements. It is also seen to perform better predictively in $\sigma_c < 80$ MPa, than it does at higher stress levels.

The fitting success of the model is undoubtedly determined to a large extent by its assumptions. To explain its inability to capture the observed kinks in the strain measurements, we hypothesize that they have their origins in the statistical variation of the frictional threshold along the interface, which if large enough may cause localized stick-slip relative motions across the interface in regions of marked interfacial weakness. These may in turn severely perturb the interfacial shear stress profile, and therefore, the measurements. This is contrary to the assumption of a constant frictional threshold of the interface τ^* in the model. This hypothesis may be confirmed by comparing the available measurements with another test on a nominally identical specimen. Scatter between the two measurements, comparable to the kinks observed would indicate correctness of the hypothesis. While the present model may be adapted to include large variations in the strength of the interface, doing so may be uninteresting from a practical standpoint. For, in a large multi-fiber composite

the effect of such variability will likely be averaged out unless it is so strong as to initiate damage that propagates (Mahesh *et al* [2]). As for the deterioration of the model's predictions for $\sigma_c \geq 80$ MPa, we attribute it to the elasto-plastic constitutive model assumed. A flow theory [14] based model of matrix plasticity may need to be incorporated if the errors committed by the present model are judged excessive at the highest load for a particular application. This modification, which will considerably increase the computational cost of the model, will be needed if the maximum applied load is such that matrix elements in the composite go far into the plastic regime.

We have attributed the prediction errors of the present model largely to the constitutive assumptions of its constituents and not so much to its essential one-dimensional character. This assertion represents our untested intuition, and will require an axisymmetric numerical calculation such as that described in Section 1 for verification. Also as mentioned in Section 1, extension of the ideas presented here to a multi-fiber composite model analogous to the extension of Cox's [3] model to Hedgepeth's [9] represents another future goal.

Acknowledgements

This study was supported by the National Science Foundation (CAREER grant no. DMR-9985264) at Caltech and a Laboratory-Directed Research and Development Project (no. 2000043) at Los Alamos.

References

[1] Hanan J. C., Mahesh S., Üstündag E., Beyerlein I. J., Swift G. A., Clausen B., Brown D. W., and Bourke M. A. M., 2003. Strain evolution after fiber failure in a single fiber metal matrix composite under cyclic loading. *Submitted to Mat. Sci. Engng. A*.

[2] Mahesh S., Phoenix S. L., and Beyerlein I. J., 2002. Strength distributions and size effects for 2D and 3D composites with Weibull fibers in an elastic matrix. *Int. J. Fract.*, 115, 41–85,

[3] Cox H. L., 1952. The elasticity and strength of paper and other fibrous materials. *Br. J. Appl. Phys.*, 3, 72–79.

[4] Aveston J., and Kelly A., 1973. Theory of multiple fracture of fibrous composites. *J. Mater. Sci.*, 8, 352–362.

[5] Budiansky B., Hutchinson J. W., and Evans A. G., 1986. Matrix fracture in fiber-reinforced ceramics. *J. Mech. Phys. Solids*, 34(2):167–189.

[6] Hsueh C-H. 1990. Interfacial debonding and fiber pull-out stresses of fiber-reinforced composites. *Mater. Sci. Eng.*, A123, 1–11.

[7] Hsueh C-H. 1992. Interfacial debonding and fiber pull-out stresses of fiber-reinforced composites: Part 7. *Mater. Sci. Eng.*, A154, 125–132.

[8] Hsueh C. H., Young R. J., Yang X., and Becher P. F., 1997. Stress transfer in a model composite containing a single embedded fiber. *Acta mater.*, 45(4):1469–1476.

[9] Hedgepeth J. M. 1961. Stress concentrations in filamentary structures. Technical Report TND-882, NASA.

[10] Hedgepeth J. M., and Van Dyke, P. 1967. Local stress concentrations in imperfect filament composites. *J. Compos. Mater.*, 1, 294–309.

[11] Landis C. M., and McMeeking, R. M., 1999. A shear-lag model for a broken fiber embedded in a composite with a ductile matrix. *Compos. Sci. Tech.*, 59, 447–457.

[12] Lagoudas D. C., Phoenix S. L., and Hui, C-Y. 1989. Time evolution of overstress profiles near broken fibers in a composite with a viscoelastic matrix. *Int. J. Solids Structures*, 25, 45–66.

[13] Beyerlein, I. J., and Phoenix, S. L., 1998. Time evolution of stress redistribution around multiple fiber breaks in a composite with viscous and viscoelastic matrices. *Int. J. Solids Structures*, 35, 3177–3211.

[14] Hill, R, 1950. *The mathematical theory of plasticity.* Clarendon Press, Oxford.

[15] Budiansky, B, 1959. A reassessment of deformation theories of plasticity,. *J. Appl. Mech.*, 259–264.

[16] Roberts, S. M., and Shipman. J. S., 1972. *Two-point boundary value problems: shooting methods.* American Elsevier Pub. Co, New York.

[17] Collatz, L., 1960. *The numerical treatment of differential equations.* Springer-Verlag, Berlin.

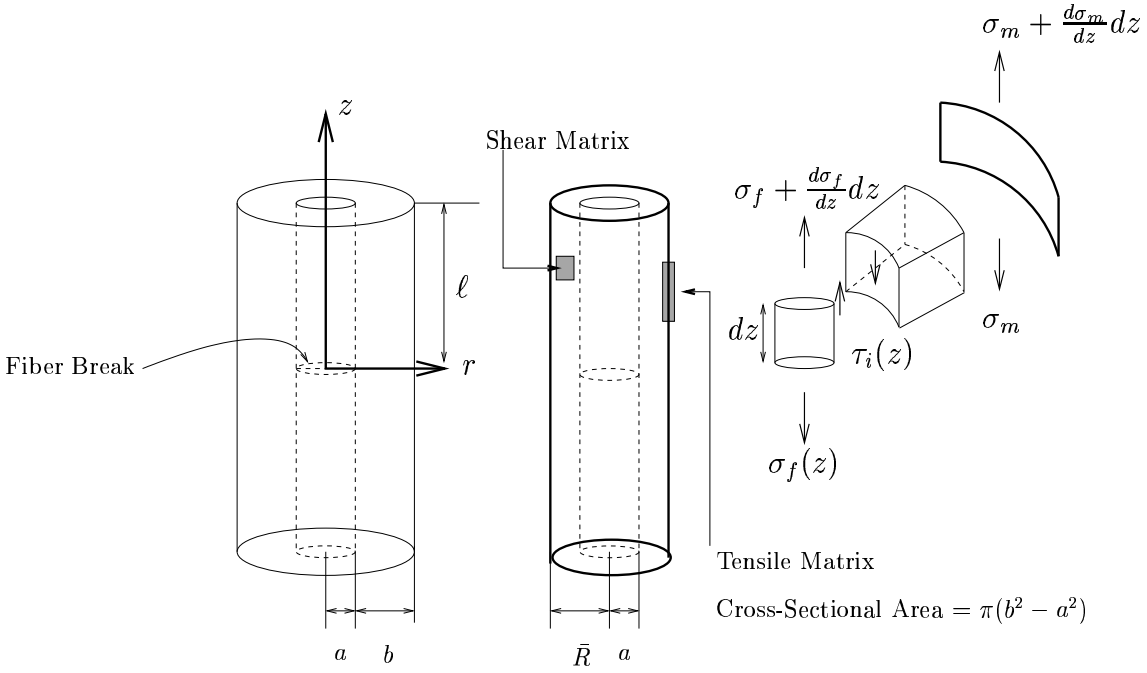

Fig. 1. Geometry of the single fiber shear lag model (after Budiansky *et al* [5]). (a) The composite cylinder, (b) the idealized model composite with the matrix divided into distinct tensile and shear parts, and (c) axial and shear stresses in representative elements of the fiber, shear matrix and tensile matrix.

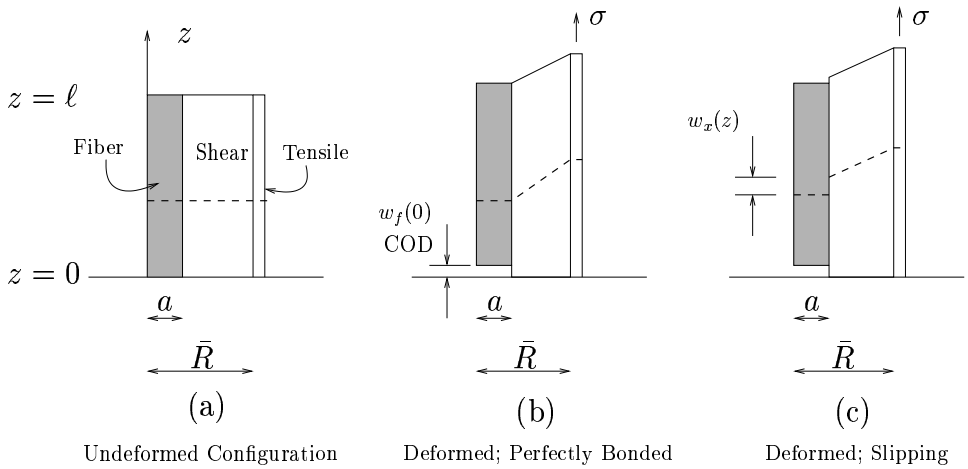

Fig. 2. Schematic depicting the notion of the slip displacement $w_x(z)$. (a) The fiber, shear matrix and the tensile matrix in the undeformed configuration. The tensile matrix is shown with finite width for clarity. A "scratch" along $z =$ constant is also shown as a dotted line. (b) The displacement of the model composite constituents upon loading with a perfect non-debonding interface shows the continuity of the "scratch" across the fiber/shear matrix interface. (c) When the interface slips however, the scratch becomes discontinuous, and the discontinuity as shown is taken as $w_x(z)$.

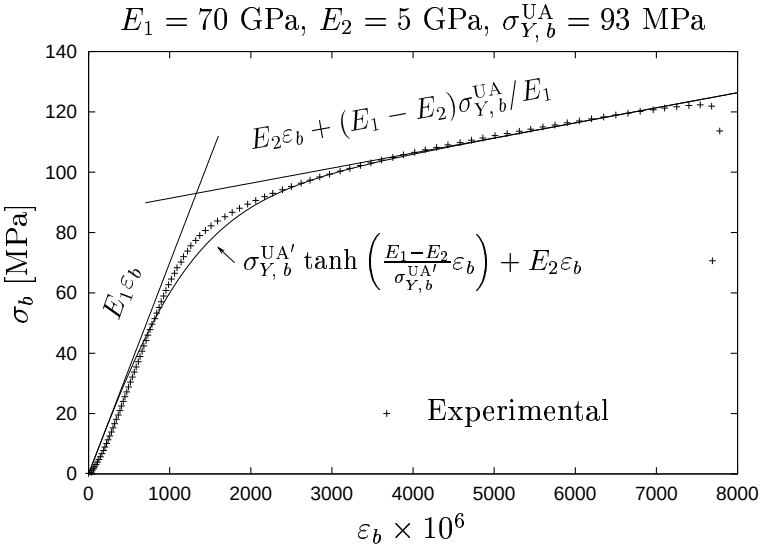

Fig. 3. The bulk (monolithic) stress-strain (σ_b-ε_b) curve of Al 6061 used as the matrix material in the experiment described in Section 4. The two branches of the bilinear approximation Eq. (7) and the smooth approximation Eq. (9) are also shown.

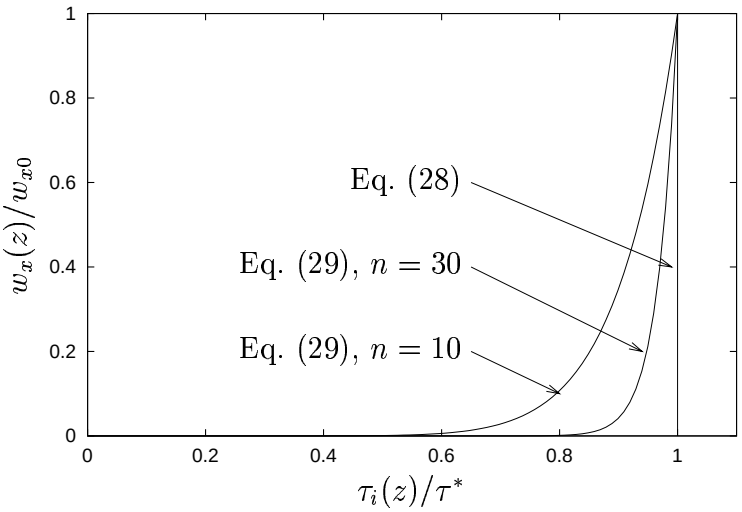

Fig. 4. Comparison of the usual (e.g., Budiansky *et al* [5]) interfacial slip condition Eq. (28) with the regularized form Eq. (29) assumed in this work.

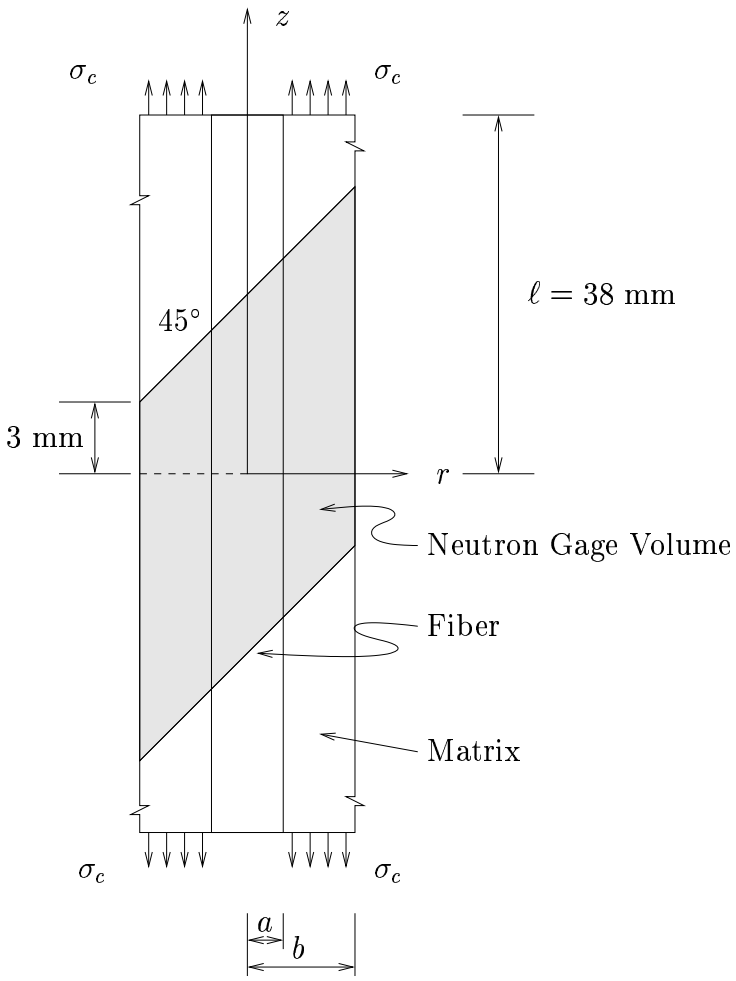

Fig. 5. Geometry of the test specimen and the neutron gage volume. a and b denote the fiber and composite radii, respectively. Stress is applied only to the matrix as shown.

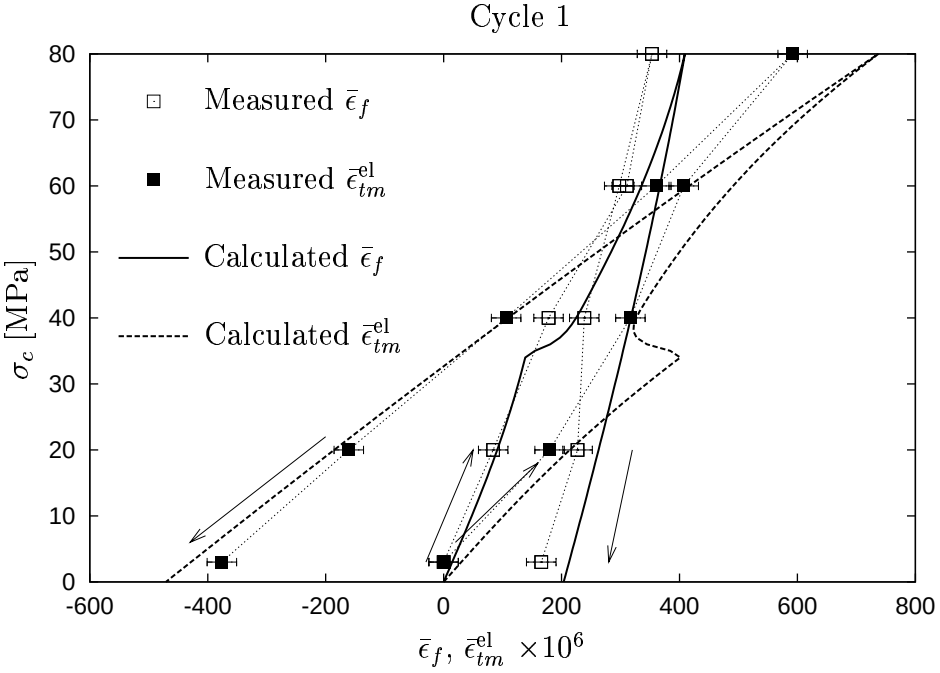

Fig. 6. Comparison of the predicted fiber and matrix average strains with those measured during cycle 1 of the cyclic tension test described by Hanan *et al* [1]. A 25×10^{-6} error bar is shown around each of the experimental points.

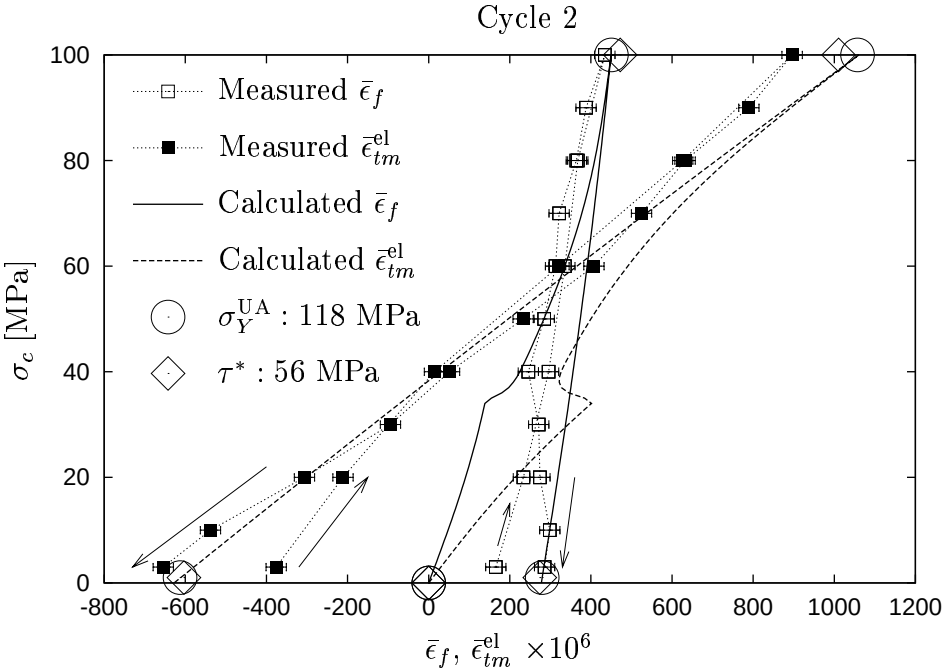

Fig. 7. Comparison of the predicted fiber and matrix average strains with those measured during cycle 2 of the cyclic tension test described by Hanan *et al* [1]. A 25×10^{-6} error bar is shown around each of the experimental points. The sensitivity of the model to each of the parameters $\sigma_Y^{\rm UA}$ and τ^* is also shown by plotting the peak and residual strains calculated by slightly increasing only that parameter over its value (Table 1) used in the main fit. $\sigma_Y^{\rm UA}$ is increased from 108 to 118 MPa, and τ^* from 51 to 56 MPa.

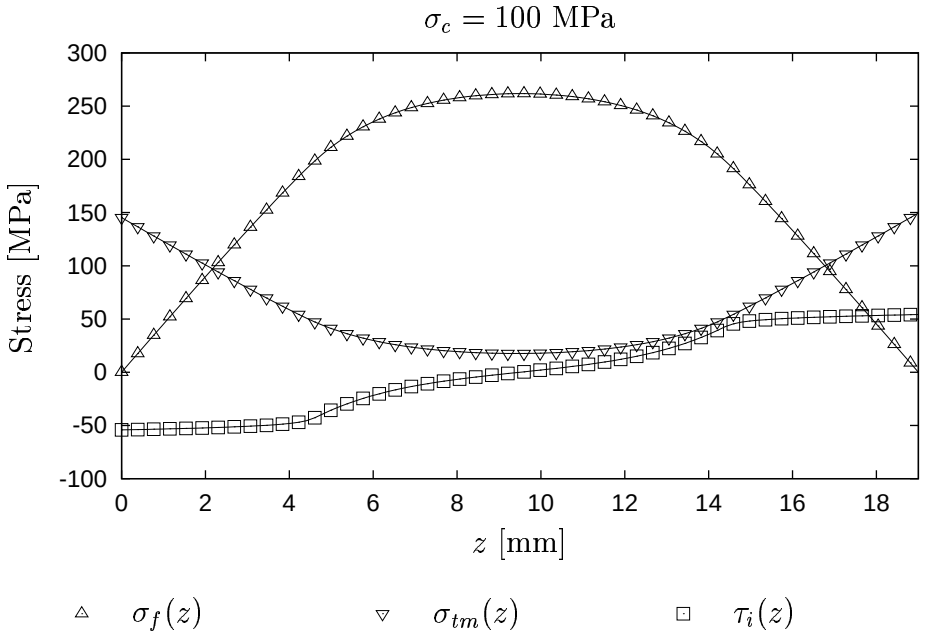

Fig. 8. Calculated axial stress profile in the fiber ($\sigma_f(z)$), tensile matrix ($\sigma_{tm}(z)$), and interfacial shear ($\tau_i(z)$) at the peak load $\sigma_c = 100$ MPa.

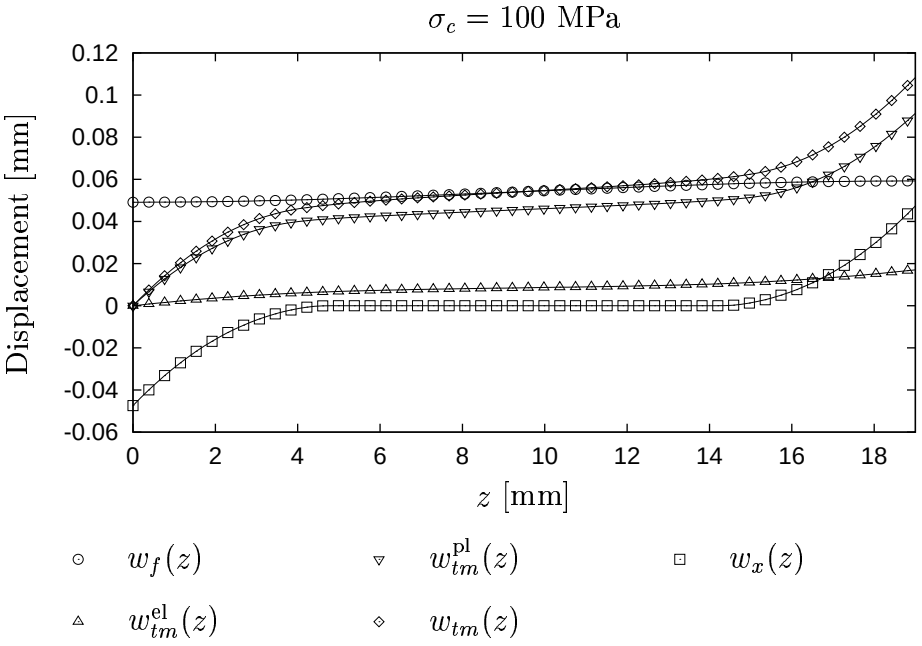

Fig. 9. Calculated axial displacement profiles of the fiber ($w_f(z)$), of the tensile matrix (elastic ($w_{tm}^{\mathrm{el}}(z)$), plastic ($w_{tm}^{\mathrm{pl}}(z)$) and total ($w_{tm}(z)$)), and the interfacial slip displacement ($w_x(z)$) at the peak load $\sigma_c = 100$ MPa.

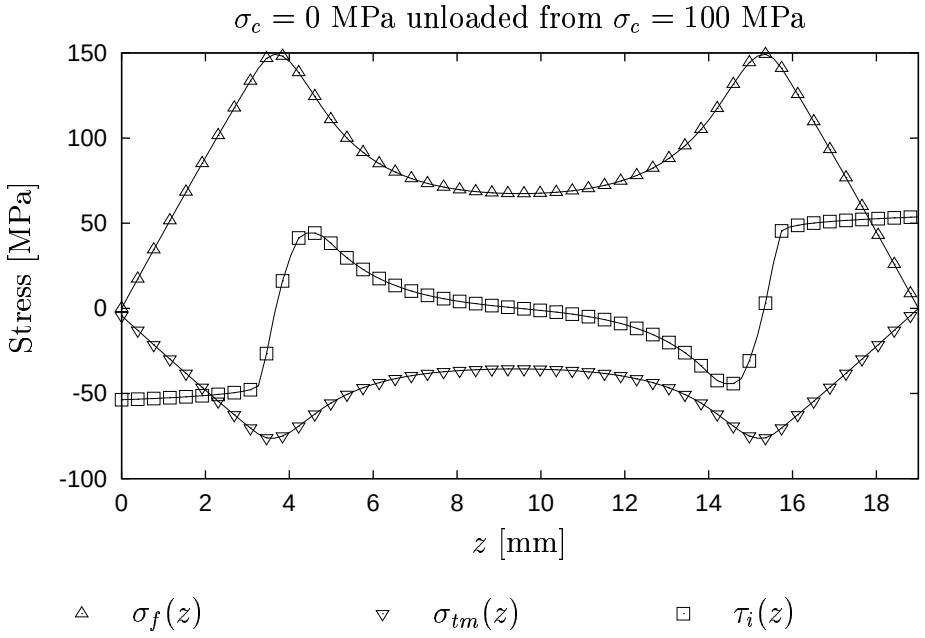

Fig. 10. Calculated axial stress profile in the fiber ($\sigma_f(z)$), tensile matrix ($\sigma_{tm}(z)$), and interfacial shear ($\tau_i(z)$) upon unloading to $\sigma_c = 0$ MPa from a peak load of $\sigma_c = 100$ MPa.

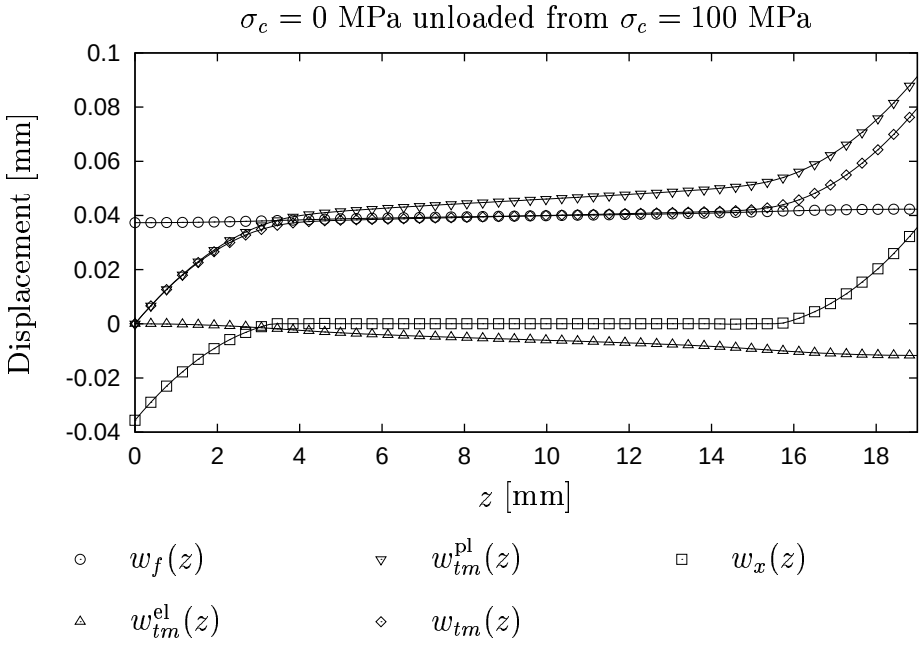

Fig. 11. Calculated axial displacement profiles of the fiber ($w_f(z)$), of the tensile matrix (elastic ($w_{tm}^{\mathrm{el}}(z)$), plastic ($w_{tm}^{\mathrm{pl}}(z)$) and total ($w_{tm}(z)$), and the interfacial slip displacement ($w_x(z)$) upon unloading to $\sigma_c = 0$ MPa from a peak load of $\sigma_c = 100$ MPa.

E_f	330 GPa	σ_Y^{UA}	108 MPa
E_1	70 GPa	τ^*	51 MPa
E_2	5 GPa	w_{x0}	0.01 mm
G_1	27 GPa	a	2.375 mm
G_2	3.2 GPa	b	4.125 mm
n	30	$\bar{R}$	3.25 mm

Table 1
Constants used in the model. Only τ^*, and σ_Y^{UA} are fitting parameters which were not measured. The material parameters E_f, E_1, E_2 were measured on bulk samples of the fiber and matrix materials (see Hanan *et al* [1]), G_1, and G_2 were deduced therefrom in Section 2.2, and w_{x0} and n were chosen based on computational considerations.